Journal of Materials Chemistry A

ROYAL SOCIETY OF CHEMISTRY

PAPER

View Article Online
View Journal | View Issue

Cite this: J. Mater. Chem. A, 2024, 12, 5282

Design, synthesis and characterization of hierarchical porous stacked thin films based on MOFs and ordered mesoporous oxides†

Melina Arcidiácono, [a] Juan A. Allegretto, [ab] Omar Azzaroni, [a] Paula C. Angelomé *[c] and Matías Rafti *[a]

Received 25th October 2023
Accepted 12th January 2024

DOI: 10.1039/d3ta06529d

rsc.li/materials-a

Sub-micrometre thin alternate bilayers of materials with appropriate refractive index contrast are widely used for the assembly of sensors based on the stimuli-responsiveness of such 1D photonic crystals (PC). A new degree of complexity was recently enabled by the availability of highly ordered multiporous materials. Specifically, we studied the integration of two kinds of materials with different refractive indexes: Si- and Ti-based highly ordered mesoporous oxides with defined pore sizes, and both Zr- and Zn-based Metal Organic Frameworks (UiO-66 and ZIF-8 MOFs), featuring microporosity and chemically tunable affinity. Synthesis conditions must guarantee the preservation of structural and chemical integrity when both building blocks are assembled into bilayers. Thus, we studied the influence of usually employed synthetic procedures for the selected individual materials on the available porosity, crystalline structure, and morphology of the obtained bilayers, and propose suitable paths for the integration of multilayers capable of acting as 1D-PCs with both meso- and microporosity.

1. Introduction

Vibrant and attractive colours ubiquitously observed in nature arise not only from chemical composition, but also from the presence of ordered nanostructures known as Photonic Crystals (PCs), where the periodic variation of the refractive index (RI) produces colour as a result of constructive interference of light shining on them.[1,2] Periodic variation of RI as a result of the nanostructure can extend from one- to three-dimensions, thus generating 1D- to 3D-PCs.[3,4] These nanostructures have been employed over the last few decades in many different fields, given their ability for transducing perturbations into an optical readout. Interesting examples include the use of polymeric materials for the assembly of optical sensors featuring RI variation when exposed to, *e.g.*, electric, magnetic, chemical, or mechanical perturbations.[5] A popular strategy for conferring responsiveness is to replace bulk oxides with porous materials, which, due to capillary condensation, trigger a measurable RI change.[6–8] Similarly as in distributed Bragg stacks or DBRs, one of the most promising options in this regard are 1D-PC vapour sensors based on mesoporous oxide thin films (MTFs).[9–11] MTFs are prepared by depositing a solution that contains an oxide precursor and an amphiphilic molecule, either *via* spin or dip coating, that during deposition and through self-assembly acts as supramolecular template.[12] The oxide, on the other hand, is formed through sol–gel reactions. Once the template is eliminated either by solvent extraction or thermal treatment, tunable thickness films showcase an ordered array of mesopores with also tunable diameters in the range of 2–10 nm.[13–16] Although the use of MTFs for DBRs brings the interesting possibility of size-exclusion, there are still obvious drawbacks caused by the lack of selectivity arising from: (i) similar affinities of usually targeted analytes with common MTFs and (ii) similar RI of the targeted analytes. Improvements have been proposed in this regard, for example, the implementation of chemically modified sensor arrays with different responses producing a unique output for a given analyte, *i.e.*, chemical noises.[17–19]

An increasingly popular alternative employed to circumvent the above discussed shortcomings is to enrich structural and chemical tunability of 1D-PCs through the inclusion of porous materials belonging to the well-established family known as Metal Organic Frameworks (MOFs).[20] MOFs are materials based on the non-covalent combination of metallic ions and multidentate organic linkers into 3D ordered structures that feature permanent porosity. Since the appearance of pioneering studies reporting their interesting adsorption properties,[21,22] MOFs have raised an ever-increasing interest due to a myriad of

[a]Instituto de Investigaciones Fisicoquímicas Teóricas y Aplicadas (INIFTA), Departamento de Química, Facultad de Ciencias Exactas, Universidad Nacional de La Plata, CONICET, CC 16 Suc. 4, B1904DPI, La Plata, Argentina. E-mail: mrafti@quimica.unlp.edu.ar

[b]Laboratory for Life Sciences and Technology (LiST), Department of Medicine, Faculty of Medicine and Dentistry, Danube Private University, 3500 Krems, Austria

[c]Gerencia Química & INN, Centro Atómico Constituyentes, Comisión Nacional de Energía Atómica, CONICET, Av. General Paz 1499, 1650, San Martín, Buenos Aires, Argentina. E-mail: angelome@cnea.gov.ar

† Electronic supplementary information (ESI) available. See DOI: https://doi.org/10.1039/d3ta06529d

possible applications in diverse fields such as separation, catalysis, sensing, energy, or drug delivery, just to mention some of the most relevant examples.[23–29,77] The potential of MOFs as building blocks for optical sensors and PCs has not gone unnoticed.[30] Following the seminal contribution by Hupp *et al.* of a Fabry-Pèrot MOF-based vapour sensor,[31] research efforts along this line have increased substantially; interesting reports include direct nanoparticle self-assembly for RI contrast,[32–35] and filling or imprinting strategies for the nanofabrication of patterned surfaces acting as 2D-PCs.[36–38] Due to the nature of building blocks, when employing MOFs for the assembly of 1D-PCs, additional materials must be included in order to guarantee the necessary RI periodic variation. Such RI contrast has been achieved by combining bilayers of MOFs and dense oxide nanoparticles or films (typically SiO_2 or TiO_2).[39–43] However, the combination of MOFs with highly ordered surfactant-templated MTFs such as those obtained *via* sol–gel chemistry bears the potential for constituting a new generation of 1D-PCs but remains virtually unexplored. For such an end, if multiple bilayers are to be integrated into photonic nanoarchitectures, the (unfortunately not straightforward) compatibility requirement between synthetic routes for both materials must be met. This is an essential step towards the rational organization of nanostructures into functional materials, *i.e.*: "*nanoarchitectonics*".[44,45] Template-extraction and calcination steps required for MTFs might irreversibly affect the MOF phase; and conversely, MOF synthesis conditions typically involve organic solvents and/or strong acid modulators that might cause disruption of the MTF structure *via* template extraction or induce further changes through dehydration of metal oxide/oxyhydroxide moieties. Preparation methods must also ensure the necessary stratification and controlled thickness of alternate stacks, avoiding, for example, interpenetration generated by cross-diffusion of precursors. Aiming to identify strategies yielding bilayers and employing archetypal materials of each class, we explored the synthesis of bilayers composed of TiO_2- and SiO_2-based MTFs with different pore sizes[13] and combined them with two selected MOFs, namely, Zr-benzene dicarboxylic acid-based UiO-66[46] and Zn-methylimidazolate-based ZIF-8.[47] We were able to identify critical steps and adapt typical synthetic procedures employed for the selected individual building blocks to preserve structural integrity. Evaluation was carried out in terms of key parameters such as available porosity, structure, and crystallinity. Finally, bilayers were assembled using building blocks in different orders, adapted protocols for template extraction and calcination procedures for mesoporous oxides, and synthesis/purification methods for MOFs to identify appropriate routes that would be feasible for the fabrication of multiporous 1D-PCs.

2. Materials and methods

Anhydrous methanol was obtained from commercial methanol as previously reported.[48] Zinc nitrate hexahydrate ($Zn(NO_3)_2 \cdot 6H_2O$), 2-methylimidazole (HmIm), (3-aminopropyl)triethoxysilane (APTES), $ZrCl_4$, terephthalic acid (benzenedicarboxylic acid or BDC), tetraethyl orthosilicate (TEOS), diblock copolymer Brij 58 and triblock copolymer Pluronic F127 were purchased from Sigma-Aldrich and used without further purification. $TiCl_4$ was obtained from Merck and diluted in ethanol (Biopack) before its use. *N*,*N*-Dimethylformamide (DMF) was purchased from Biopack and used without further purification. Acetic acid (AcOOH) was purchased from Anedra and used without further purification. Silicon ⟨100⟩ wafers were purchased from PhotonExport.

2.1 Single layers

2.1.1 Synthesis of mesoporous thin films (MTFs): TB, TF and SB. Sols used to deposit MTFs were prepared according to previous reports. For TiO_2 films templated with diblock copolymer Brij 58 (denominated TB) the precursor was $TiCl_4$ and the final molar proportions were: $TiCl_4$ 1 : Brij 58 0.05 : ethanol 40 : H_2O 10.[49] When F127 was used as the template (denoted as TF), the final proportions of the sol were: $TiCl_4$ 1 : F127 0.005 : ethanol 40 : H_2O 10.[50] Finally, for SiO_2 films, Brij 58 was used as the template and TEOS as the silicon source. In this case, the final molar proportions of the sol were: TEOS 1 : Brij 58 0.05 : ethanol 24 : HCl 0.28 : H_2O 5.2 (denoted as SB).[51] In all cases, sols could be used immediately after preparation and be reused if kept in a −18 °C freezer.

A defined volume (ranging from 75 to 100 microliters, depending on the substrate size) was deposited by spin coating at 4000 rpm over silicon or glass substrates previously cleaned with acetone and dried with air. Immediately after deposition, the films were subjected to a stabilisation process consisting of the following consecutive steps: 30 minutes in a 50% relative humidity chamber (obtained using a saturated solution of $Ca(NO_3)_2$), 30 minutes in an oven at 60 °C, 30 minutes in an oven at 130 °C and finally 30 minutes in an oven at 200 °C. The elimination of the template was performed either by extraction for 48 h with ethanol (films hereafter referred to as X – 200 + EE) or calcination at 350 °C for 2 hours, using a 1 °C min^{-1} ramp (hereafter referred to as X – 350).

APTES grafting of TB films was performed using a vapour-phase approach. The films were arranged in a 10 mm Petri dish box and an aluminium container filled with 500 microliters of APTES was placed alongside. Then, the box was covered and let to react for 20 minutes. After reaction, the films were placed for 15 minutes in an oven at 60 °C for thermal annealing.[52]

2.1.2 Synthesis of ZIF-8 films by liquid-phase epitaxy (LPE). Substrate preparation of silicon wafers of 95 mm diameter cut into 1.5 × 1.5 cm slides was carried out as follows: a cleaning step with acid piranha 1(H_2SO_4 98%) : 1(H_2O_2 30%) volume ratio until bubbling stopped, followed by Milli-Q water rinsing and drying with air. APTES functionalization was carried out using the same procedure described for TB films (see above). ZIF-8 films were prepared following a previously reported procedure,[48,53,54] briefly, substrates were placed into 10 mL beakers with the functionalized surface facing down, and then they were covered completely with 5 mL of 25 mM $Zn(NO_3)_2 \cdot 6H_2O$ methanolic solution. After 5 minutes, 5 mL of 50 mM HmIm was added and gently mixed to be homogeneous. After 30 minutes, the silicon substrate was taken out and carefully

washed drop by drop with methanol, and then dried with compressed air. By repetition of these steps, collectively called "growth cycles" the thickness of the film can be increased. Films grown by using this method are referred to as *n*x-ZIF-8 LPE, where *n* represents the number of growth cycles.

2.1.3 Synthesis of ZIF-8 films by spin coating (SC). Spin coating of ZIF-8 films was carried out using colloidal dispersions of nanoparticles synthesised through a slightly modified procedure compared to what is reported in recent literature.[55] Briefly, equal volumes of methanolic solutions of 25 mM $Zn(NO_3)_2$. $6H_2O$ and 100 mM of HmIm were mixed for a final molar ratio of (1 : 4 : 2000) at 25 °C. After 3 hours, ZIF-8 nanoparticles were separated from the mother liquor by centrifugation at 11 400 rpm for 10 minutes. The solid was then redispersed in fresh methanol and centrifuged again to complete two purification cycles. Subsequently, ZIF-8 nanoparticles were redispersed in 1.5 mL methanol and employed for spin coating. The standardised process and complete characterization of the material obtained are presented in the ESI (see Section S1†). Films were assembled on APTES-modified silicon substrates by casting 0.1 mL ZIF-8 dispersion for 1 min while the substrate was spun at 1200 rpm and dried with compressed air. These steps constitute one "deposition cycle"; by performing ten cycles (10x-ZIF-8 SC), films with a typical thickness of 400 nm were obtained.

2.1.4 UiO-66 films by liquid-phase epitaxy (LPE). UiO-66 films were synthesised according to previously reported procedures.[56,57] Briefly, silicon substrates were cleaned as described above and then placed horizontally in a beaker and covered with 33 mM solution BDC in DMF for three days at room temperature. After this surface modification step, substrates were placed vertically in sealed Schlenk tubes and covered with UiO-66 precursors solutions in the following molar ratio Zr 1 : BDC 1 : H_2O 1 : AcOOH 500 : DMF 1500 and placed in an oven at 120 °C for 24 hours. Finally, the samples were cleaned with fresh DMF and dried at 120 °C overnight.

2.2 Integration strategies for bilayers (layer contacting the substrate/layer deposited on top)

2.2.1 MOF/MTF bilayers. Mesoporous thin films were deposited on MOF covered substrates using the same approach described for the MTF single layer preparation, performing the thermal treatment until 200 °C, to prevent thermal degradation of MOFs.[47,58–61]

2.2.2 MTF/ZIF-8 LPE bilayers. LPE growth of ZIF-8 was conducted on mesoporous films using a similar approach described for MOF single layers: here, the mixture with MOF precursors was let to evolve for five minutes before placing the MTF modified substrate vertically in the reaction beaker.

2.2.3. MTF/ZIF-8 SC bilayers. ZIF-8 nanoparticles were spin coated on mesoporous films using the same approach described for MOF single layers.

2.2.4. MTF/UiO-66 LPE bilayers. LPE growth of UiO-66 films was conducted using the same approach described for MOF single layers.

2.3. Characterization

Atomic Force Microscopy (AFM) measurements were performed using a Keysight 9500 microscope in AC mode within a dry environment. The probes employed included Tap190-G, Multi75Al-G, and Tap150Al-G.

Ellipsometry experiments were carried out using a Woolan Alpha-SE Spectroscopic Ellipsometer equipped with a CCD detector and rotatory compensator (spectral range: 380–900 nm), at 70° incidence angle.

X-Ray Reflectometry (XRR) and X-Ray Diffraction (XRD) measurements were performed using a PanAlytical Empyrean diffractometer using a dedicated thin film optic, with an incident beam of Cu K_α radiation (1.54 Å). For XRR, a 1/32° divergence slit and a 0.18 mm receiving slit were mounted. Measurements were performed in a chamber that allows the atmosphere control by either introducing silica gel (dry atmosphere) or hot water (vapour saturated atmosphere). Details about these measurements and the data processing can be found elsewhere.[62–64] The same configuration, but with a 1/16° divergence slit, was used to measure in the 2θ region corresponding to the mesoporous order peak (2–5° 2θ). Grazing incidence (GI-XRD) measurements, on the other hand, were performed with incidence fixed at 1° and scanning the 4–10° 2θ range, using a 1/2° divergence slit and none receiving slit.

Scanning Electron Microscopy (SEM) measurements were performed using Zeiss Crossbeam 340 Gemini equipment. Samples were cut into small pieces and fixed to an aluminium stub using conductive carbon tape. Transmission Electron Microscopy (TEM) measurements were performed using a Philips CM 200 microscope operated at 160 kV. Samples were scratched from the substrate using a scalpel and the obtained powder was deposited onto a FORMVAR and carbon-coated Cu grid. Dynamic Light Scattering (DLS) measurements were carried out using a ZetaSizer Nano-ZS90 (Malvern Instruments Ltd.). Surface area determination was carried out with an ASAP 2020 HD88 surface area and porosity analyzer (Micromeritics).

3. Results and discussion

3.1 Synthesis and characterization of single layers

As discussed thoroughly in previous sections, the combination of a microporous MOF and MTF into bilayers has the potential to yield 1D-PCs with hierarchical porosity and *ad hoc* chemical affinity. To enable such a possibility, the suitability of different strategies was explored regarding the cross-compatibility of the synthetic procedures followed. The selection made in the present work is summarised in Fig. 1. MOF films prepared either *via* LPE or SC can be combined with MTFs to get MOF/MTF or MTF/MOF bilayers (layer contacting the substrate/layer deposited on top). Each procedure for a layer growth requires specific conditions and yields a structure that will naturally affect the growth/deposition of the subsequent layer; therefore, as a first step towards bilayer design, a thorough characterization of the single layers employed was required.

It has been previously shown that continuous ZIF-8 films can be obtained using properly modified substrates, by introducing

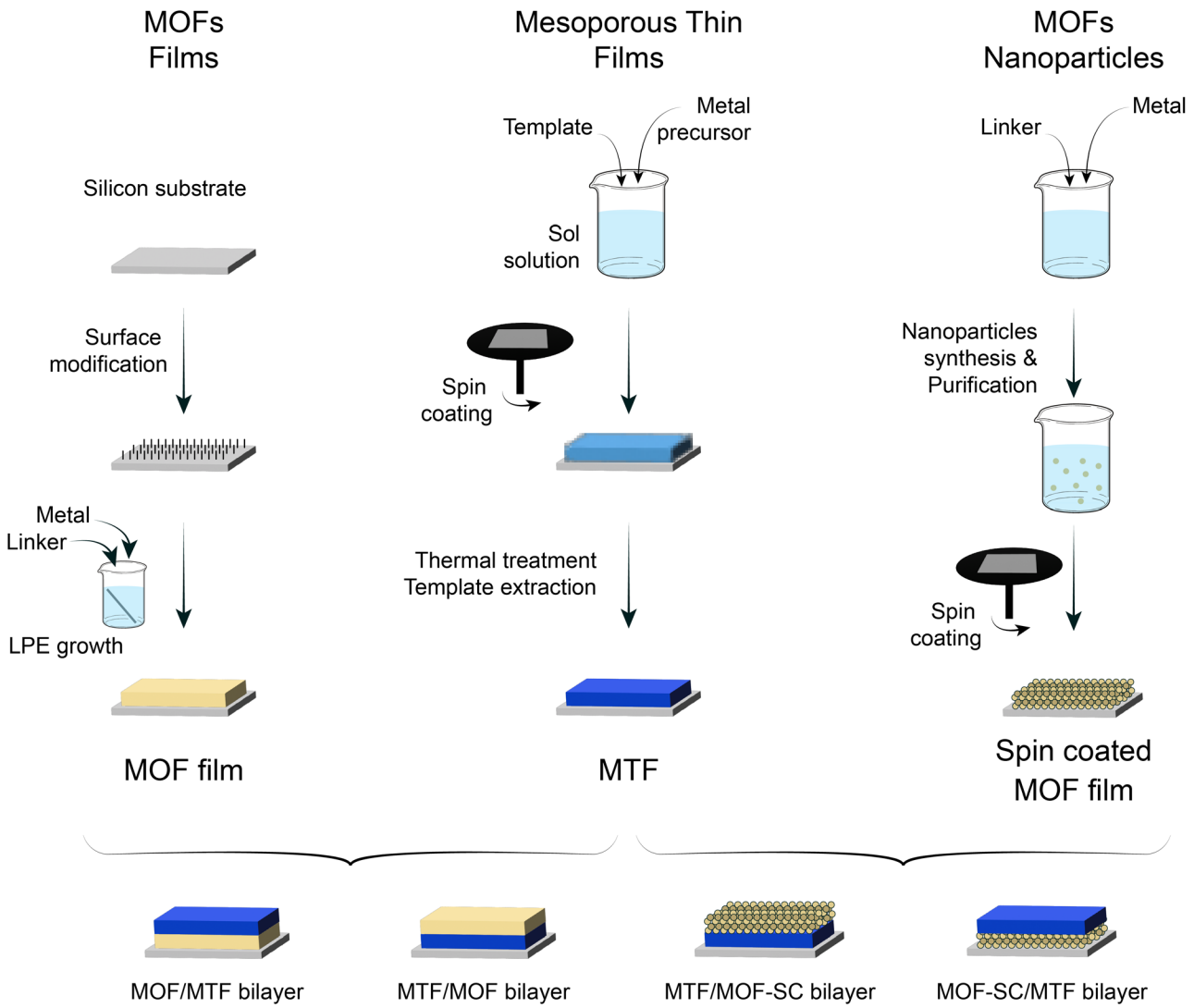

Fig. 1 Schematic representation for the obtention of LPE and SC MOF films, together with MTFs, and the combinations explored.

primer layers featuring chemical moieties capable of enhancing heterogeneous nucleation.[48] The selection of such primer as well as the grafting strategy will determine the surface density of nucleation points in the substrate and thus will affect the growth extent and final morphology of the film.[65] When using APTES as the primer, the films feature relatively high constructional porosity (CP, *i.e.*, empty spaces in the meso-scale range across the film arising from defects and gaps generated in the spots where the growth fronts coalesce) in addition to the inherent ZIF-8 MOF microporosity. CP has been shown to play a significant role in adsorption and transport properties of films.[29,66] This makes determination of the total accessible porosity far from trivial, since it includes both porous domains: intrinsic microporosity and meso-scale CP, which can even introduce domains with different specific affinities.

As can be seen in Fig. 2a(i), the (110) diffraction peak from ZIF-8 is present at $2\theta = 7.35°$, meaning that the native microporous structure of the MOF is present. It is worth noting that due to its low thickness (153 nm value was determined with ellipsometry for 5x-ZIF-8 LPE, see Section S2, ESI†) diffraction peaks corresponding to the 1x-ZIF-8 LPE film are not visible, and thus there is a necessity of performing XRD using thicker 5x-ZIF-8 LPE films. Nevertheless, 1x-ZIF-8 LPE could be used to measure XRR patterns. The critical angle measured by XRR is defined as the 2θ value for which the intensity of reflected X-rays is reduced to half of the maximum and can be directly related to the electronic density of the film.[67] Thus, by comparing values corresponding to dry and water-saturated atmospheres, it was possible to analyse water-accessibility of the material. For ZIF-8, given the intrinsic hydrophobic nature of microporosity, the variation observed accounts for the accessible and more hydrophilic CP (see discussion below). In the same way, XRD and XRR experiments were conducted on ZIF-8 SC films as shown in Fig. 2b, which also showed the characteristic (110) diffraction peak and critical angle, denoting the presence of the synthesised material. For the case of the UiO-66 LPE film (Fig. 2c), XRD revealed a preferential orientation of the (111) plane, in line with previously reported results.[68] Furthermore,

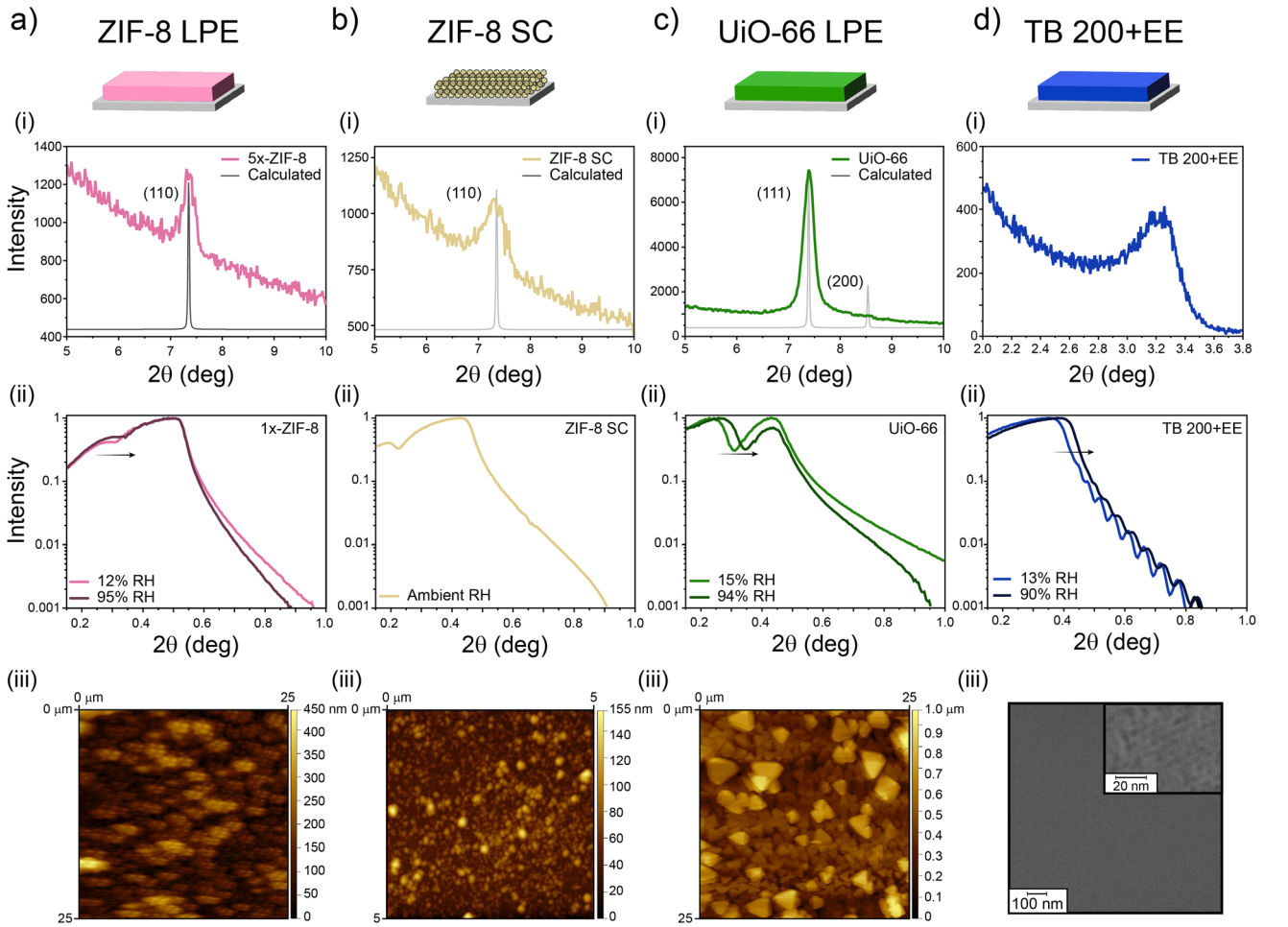

Fig. 2 Characterization of (a) ZIF-8 films grown by the LPE method (ZIF-8 LPE); (b) ZIF-8 films assembled by spin-coating of nanoparticles (ZIF-8 SC); (c) UiO-66 films grown by the LPE method (UiO-66 LPE); (d) TiO_2 mesoporous films obtained using Brij 58 as the template and maximum 200 °C processing temperature (TB 200+EE): (i) XRD and (ii) XRR in dry and water-saturated atmospheres together with surface analysis of the single layers by means of (a–c iii) AFM and (d iii) SEM.

the critical angle observed for the UiO-66 LPE film has a shift upon water adsorption, in line with the increased hydrophilic character of the micropores present compared with ZIF-8.[69] AFM images show a uniform MOF coverage and the morphology and size of particles (or grain boundaries arising from colliding nucleation fronts during LPE) which integrate the films. Finally, Fig. 2d shows the diffraction pattern and XRR curves for the TB 200+EE film. In this case, milder extraction protocols implemented yielded a smooth and homogeneous film, as confirmed by the presence of Kiessig fringes in the XRR pattern. The presence of a well-ordered array of mesopores is confirmed by the appearance of a diffraction peak at 3.5° 2θ in the GI-XRD pattern of the sample (Fig. 2d(i)), corresponding to a periodic arrangement of mesopores with an interplanar distance of 2.5 nm in the direction perpendicular to the substrate. The mesopores and their long-range organisation are also visible on the film surface, as denoted by the SEM image presented in Fig. 2d(iii) and S3, ESI.† XRR curves evidence a shift due to capillary condensation when using dry and vapor-saturated conditions thus confirming the accessibility of the mesopores. Similar results, regarding the MTF accessibility, were obtained for SB 200+EE, TF 200+EE and TF 350 systems, in accordance with previous reports (Fig. S4 and S5, ESI†).[49–51]

Through spectroscopic ellipsometry (SE), thicknesses and refractive indexes (corresponding to 632 nm wavelength) were determined for the films employing *ad hoc* optical models. With this information, it was possible to apply effective medium approximation to obtain total porosities.

As presented in Table 1, all single layers present thicknesses between 70 and 250 nm, but with very different refractive indexes and porosities. It is worth noting that porosity values determined after applying Bruggemann approximation on ellipsometric measurements and those determined by XRR differ from each other. In the case of the 5x-ZIF-8 LPE layer, the difference in the values resides on XRR probing only the water-accessible porosity of the layer, while the 64% porosity found by Bruggemann's approximation arises from considering both contributions, the intrinsic microporosity of ZIF-8 (hydrophobic) and the more hydrophilic constructional porosity.[54] In the case of the ZIF-8 SC layer, the high porosity value obtained

Table 1 Thickness, surface roughness, refractive index, and porosity of the films, as determined by ellipsometry and XRR

System	Thickness (nm)	n ($\lambda = 632$ nm)	Porosity determined by ellipsometry	Porosity determined by XRR
5x-ZIF-8 LPE	153	1.324	64%	28%
ZIF-8 SC	203	1.171	80%	—
UiO-66 LPE	250	1.620	46%	24%
TB 200+EE	135	1.643	29%	39%
TB 350	74	—	—	35%
TF	176	—	—	38%
SB	183	—	—	48%

by ellipsometric measurements points towards a less compact structure being formed; however, the interparticle space upon assembly seems to be too large to allow the capillary condensation. In fact, after exposing the film to a high RH medium during a long time, no changes in the ellipsometric signal were observed (Section S6, ESI†). In the case of UiO-66, given the more hydrophilic character of its porosity, it is likely that under 15% relative humidity conditions the porous material had adsorbed more water than the other MOF, thus hindering a larger change in electronic density upon increasing to 94% RH, which would justify the difference with the ellipsometric value found for the porosity. Also, it might be possible that not all the porosity was accessible due to occlusion of solvent or remaining reactants, despite the thorough washing and activation procedures followed. Finally, for the TB 200-EE sample, differences between the values obtained by the two techniques have been observed before for similar systems.[70] Such differences may be due to the hydration equilibrium achieved in each kind of measurement and the fact that template may remain inside the films in different amounts, depending on the extraction process and subsequent cleaning of each sample. Nevertheless, the pore accessibility of TB 200-EE is high enough to ensure its use as a component of optical devices. TB 350, TF and SB layers were characterized by XRR, and the obtained thicknesses and porosities are in accordance with previously reported results.

Altogether, results summarised in Table 1 show that the single layers can be grown homogeneously, rendering films with very different refractive indexes and porosities, which makes their combination an attractive path towards 1D-PCs development.

3.2 Synthesis and characterization of bilayers

The first approach explored for the construction of bilayers was to combine nanoparticle-based spin-coating assembled ZIF-8 SC with mesoporous TiO_2. Usually, MTFs are treated at 300/350 °C to ensure template elimination but such temperatures are not compatible with the ZIF-8 stability. Thus, a shorter thermal treatment up to 200 °C was selected, based on previously reported protocols.[71] Bilayers were then prepared using such a low-temperature process and solvent extracted TB 200+EE layers.

As can be seen from XRR experiments presented in Fig. 3a, spin-coating allowed the assembly of ZIF-8 nanoparticles on top of the TB 200+EE film (TB 200+EE/ZIF-8 SC). The XRR curve shows the appearance of an additional critical angle below $2\theta = 0.2°$, corresponding to ZIF-8, and the conservation of both the critical angle and the Kiessig fringes from the MTF. The latter indicates that the homogeneity of the TB 200+EE film is preserved (see Fig. S7, ESI† for the full-range XRR curves). However, the critical angle attributed to ZIF-8 is much lower than the one of the single layer presented above, indicating a lower electronic density, which points towards a lower surface coverage. This might be due to the different wettability of the TB 200+EE film compared with the APTES-modified silicon substrates, thus rendering a low-density assembly of nanoparticles. GI-XRD experiments also show no diffraction peak from ZIF-8, thus supporting the formation of a thin deposit of particles. Dry and water-saturated XRR experiments reveal that the TB 200+EE film is still accessible to water (22% accessible porosity), although some reduction of this parameter is observed, probably due to the presence of the ZIF-8 crystals on the surface, that might hinder water diffusion. Moreover, the upper ZIF-8 SC layer does not take up much water, also in line with ellipsometry results (see Fig. S6, ESI†).

For the inverse configuration (ZIF-8 SC/TB 200+EE bilayer), the ZIF-8 SC layer was used as the starting point for the preparation of the MTF. Fig. 3b, shows the XRR pattern in which Kiessig fringes associated with the MTF layer (which also shows the expected diffraction peak attributed to the mesopore ordering, see Section S6, ESI†) are observed. Moreover, the MTF remains accessible to water (26% accessible porosity). In this configuration, in which the upper layer (TB 200+EE) is the one with the higher electronic density, the critical angle of the bottom layer (ZIF-8 SC) is not expected to be seen. However, there is no evidence of ZIF-8 being still present in the substrate, since no diffraction peak ascribable to it was detected, although it was clearly visible in the original single layer before MTF deposition (see Fig. 2b–i). This result suggests that adherence of the nanoparticles constituting the ZIF-8 SC single layer is compromised by the MTF synthesis procedure, regardless of the adaptations introduced for its compatibility with ZIF-8 MOF.

As an alternative, ZIF-8 layers grown by the LPE method were also explored. When starting from the TB 200+EE film, the oxide must be modified with a primer, to allow the anchoring of MOF precursors which later promote film growth. For this purpose, amino moieties (anchored using APTES) were employed as nucleation points for ZIF-8, thus generating the TB 200+EE/ZIF-

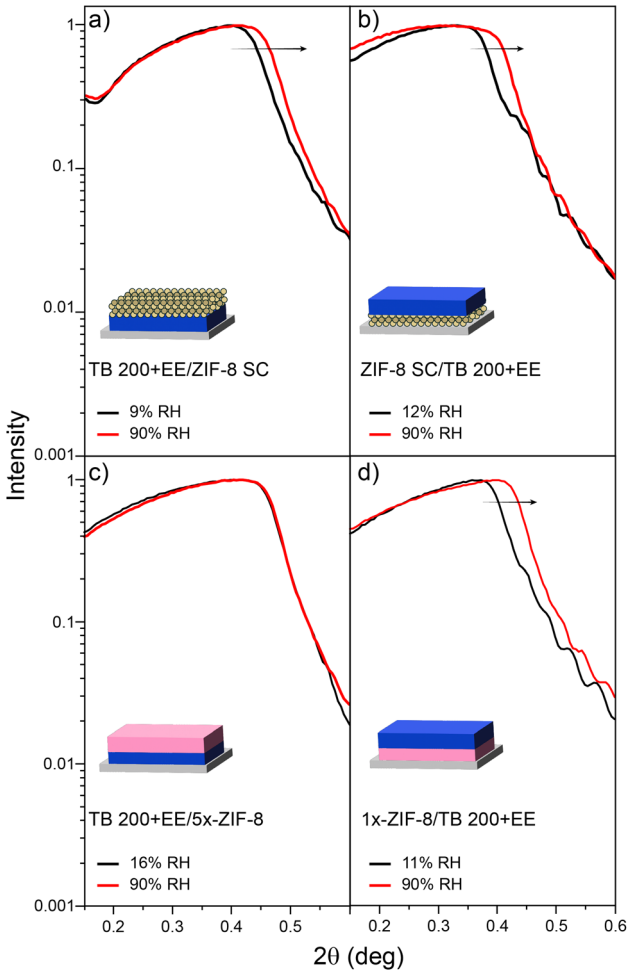

Fig. 3 XRR experiments for dry and vapour-saturated atmospheres for samples: (a) TB 200+EE/ZIF-8 SC, (b) ZIF-8 SC/TB 200+EE, (c) TB 200+EE/5x-ZIF-8 and (d) 1x-ZIF-8/TB 200+EE.

8 LPE bilayer. It was observed, however, that more than one growth cycle was needed for the presence of ZIF-8 to be detectable. By taking advantage of the progressive growth achievable *via* LPE, five growth cycles were conducted, thus generating the TB 200+EE/5x-ZIF-8 LPE bilayer. Crystallinity of the system was explored and quite interestingly a wide diffraction peak around 6.75° 2θ was observed instead of the expected peak at 7.35° 2θ. Such a result points towards the formation of a crystalline phase other than ZIF-8 due to the interactions between MOF precursors and the mesoporous film. This could also explain why when performing low- and high-moisture XRR experiments (see Fig. 3c) the porosity of the TB 200+EE layer was no longer accessible to water, since no displacement of the critical angle is observed for higher humidity. Altogether, this suggests that mesopores are being blocked by subproducts generated while attempting the synthesis of ZIF-8, blocking the access to MTF porosity. For the inverse configuration (1x-ZIF-8/TB 200+EE), again no diffraction peak for the ZIF-8 phase was observed. We hypothesise that this could be due to its low thickness, but again no structures related to ZIF-8 MOF were detected with electronic microscopy (neither SEM nor TEM). Nonetheless, a 130 nm thickness MTF film was successfully grown on the modified substrate. Such a MTF presents accessible mesopores (31% porosity, obtained from XRR shown in Fig. 3d) and an ordered pore array that gives rise to a diffraction peak at 3.25° 2θ, corresponding to an interplanar distance of 2.7 nm (see the XRD pattern in Fig. S8, ESI†).

Altogether, the formation process of the MTF seems incompatible with the production of ZIF-8/MTF bilayers and further steps are required to ensure the stability of the ZIF-8 phase (either obtained by the SC or LPE approach) during the formation of the MTF layer. Moreover, the formation of ZIF-8 over the TiO_2 porous films does not seem to occur either, even if the oxide is modified with APTES, highlighting the need of careful compatible interactions between the film and the MOF precursors.

As mentioned above, the use of different MOFs would endow the system with *ad hoc* chemical affinity, and thus is highly desirable to identify conditions for successful growth of combined MOF/MTF architectures. We have therefore explored the use of a different MOF, the Zr-based UiO-66. Differently from the single micropore size of ZIF-8, UiO-66 features two well defined micropores: a 1.1 nm wide octahedral pore and 0.8 nm wide tetrahedral pore, in a 1 : 2 ratio, connected by 0.6 nm wide windows.[72,73] This material also differs from ZIF-8 from the fact that water is capable of accessing not only the CP of the assembled film, but also the micropores.[69] Thermal and chemical stabilities of UiO-66 are also superior;[58] however, synthetic conditions require the use of strong acids as modulators, and high temperatures, which might impose a limitation for the combination with MTFs.

After conducting UiO-66 synthesis on the TB 200+EE film, the critical angle corresponding to the MOF was not visible by XRR but crystals deposited onto the mesoporous film were observed by TEM and SEM (see Section S8, ESI†). However, surface coverage was somehow low in comparison with UiO-66 grown onto the bare Si substrate. Interestingly, from the analysis of the XRR pattern, it can be concluded that the accessible porosity of the TB 200+EE after MOF growth was 44%, very similar to the value corresponding to one single layer, indicating that the UiO-66 formation does not disrupt the porosity of the bottom layer (for more information see Section S10 in ESI†).

To increase the amount of UiO-66 crystals deposited onto the MTF, TB 350 was used as a base for the MOF growth. This MTF presents a higher mechanical and chemical stability, more compatible with the UiO-66 growth conditions. In this case, UiO-66 was successfully grown on it, generating the TB 350/UiO-66 bilayer. Dry- and water-saturated XRR experiments depicted in Fig. 4a revealed that not only the mesoporosity of the TB film remains accessible (30% of porosity) after the growth of UiO-66, but also that the MOF forms a layer which is also capable of water adsorption (see Section S11† for the complete XRR range). In this case, the compactness of the UiO-66 layer is relatively low, and thus the critical angle shift cannot be observed in the same way as for the other films prepared. However, it is possible to have an estimation by analysing the shift on the minimum value in the critical angle region. By doing this, a porosity

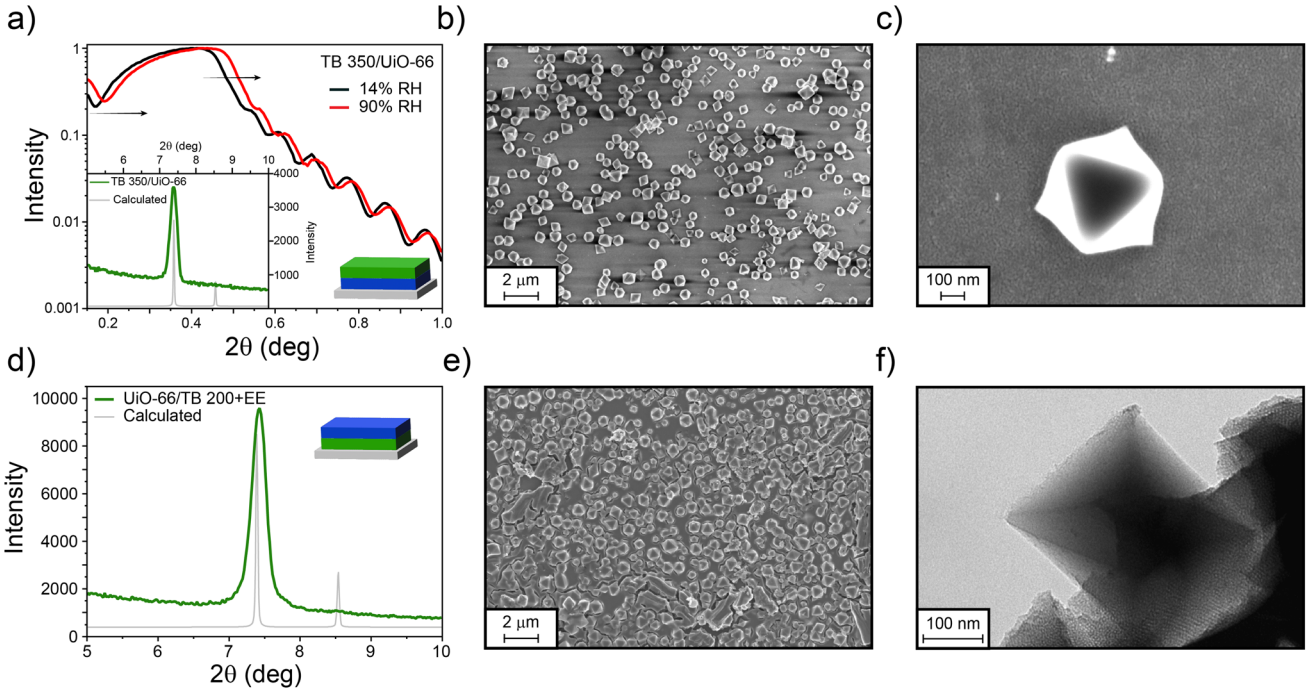

Fig. 4 (a) XRR patterns obtained in dry and water-saturated environments, (inset) XRD pattern for the TB 350/UiO-66 system, together with (b and c) SEM images. (d) GI-XRD for the UiO-66/TB 200+EE bilayer, together with (e) SEM and (f) TEM images, showing the integration of both systems.

accessible to water of about 9% can be estimated. Additionally, the XRD pattern shows the presence of the (111) diffraction peak of UiO-66, confirming its presence and preferred crystallographic orientation (see Section S11† for XRD in the complete range). SEM images (Fig. 4b and c), on the other hand, show a fair coverage of the TB surface with octahedrally shaped crystals of 500–600 nm size. The porosity of the TB 350 film can be seen in the SEM images with higher magnification (see Fig. S14, ESI†). As discussed above, and together with the information from micrographs, it is clear that UiO-66 is formed on top of the TB film and not extensively inside the mesopores, as in the case of ZIF-8. This is probably due to the specific interactions between MOF precursors and the TiO_2 matrix.

For the inverse system, TB films were synthesised on UiO-66 as for the previous examples, thus forming the UiO-66/TB 200+EE bilayer. As can be seen in Fig. 4d, and contrary to the case of ZIF-8, a strong diffraction peak from UiO-66 was visible after formation of the MTF, thus indicating the robustness of the UiO-66 film. However, and probably due to the roughness of the system, XRR measurements could not be performed. Nonetheless, the presence of both materials was also confirmed by SEM (Fig. 4e), where a continuous MTF phase is clearly visible covering the UiO-66 crystals. As the crystals are thicker than the TB film, some cracks can be observed in the surface, exposing the mesoporous film. These results are similar to those obtained when silica particles are covered by mesoporous thin films.[74] TEM images presented in Fig. 4f show that the UiO-66 crystal is clearly surrounded by the mesoporous oxide. In both configurations that combine TB films and UiO-66, the presence of MOF discrete crystals that do not completely cover the surface does not allow the determination of a single thickness for the bilayers. However, the spatial confinement of each layer is clearly demonstrated.

As mentioned before, the huge potential of this platform relies not only on the versatility rendered by the different MOFs that can be employed, but also on the fine-tuning achievable for pore sizes and the oxide employed for synthesising the MTFs. Therefore, exploring different MTFs other than TB would be of interest. Following this line of though, we have built UiO-66/MTF bilayers using the same oxide and different pore sizes (TF system, TiO_2 with interpore distance in the direction perpendicular to the substrate of about 5 nm and a pore diameter around 10 nm) and a different oxide with the same interpore distance (SB, mesoporous SiO_2). As shown in Fig. 5, both systems (UiO-66/TF 200+EE and UiO-66/SB 200+EE) were successfully obtained with the crystallinity of UiO-66 preserved. In both cases the mesoporous films covered the UiO-66 particles, once again with visible cracks as in the case of TB films. The porosity of the TF and SB layers is clearly distinguishable by TEM microscopy (see Fig. 5c and f); in the case of the TF system, the pores are ordered in the expected cubic structure[50] while in the case of SB films the pores are locally ordered. Due to the high rugosity of the samples, a thickness cannot be defined. Moreover, XRR measurements were difficult to perform. However, for the UiO-66/SB 200+EE sample a measurement could be made, as shown in Fig. S20, ESI.† Although critical angles could not be properly determined, due to the already mentioned rugosity issues, it can be clearly seen a displacement when humidity increases, thus demonstrating the accessibility of the SB 200+EE layer.

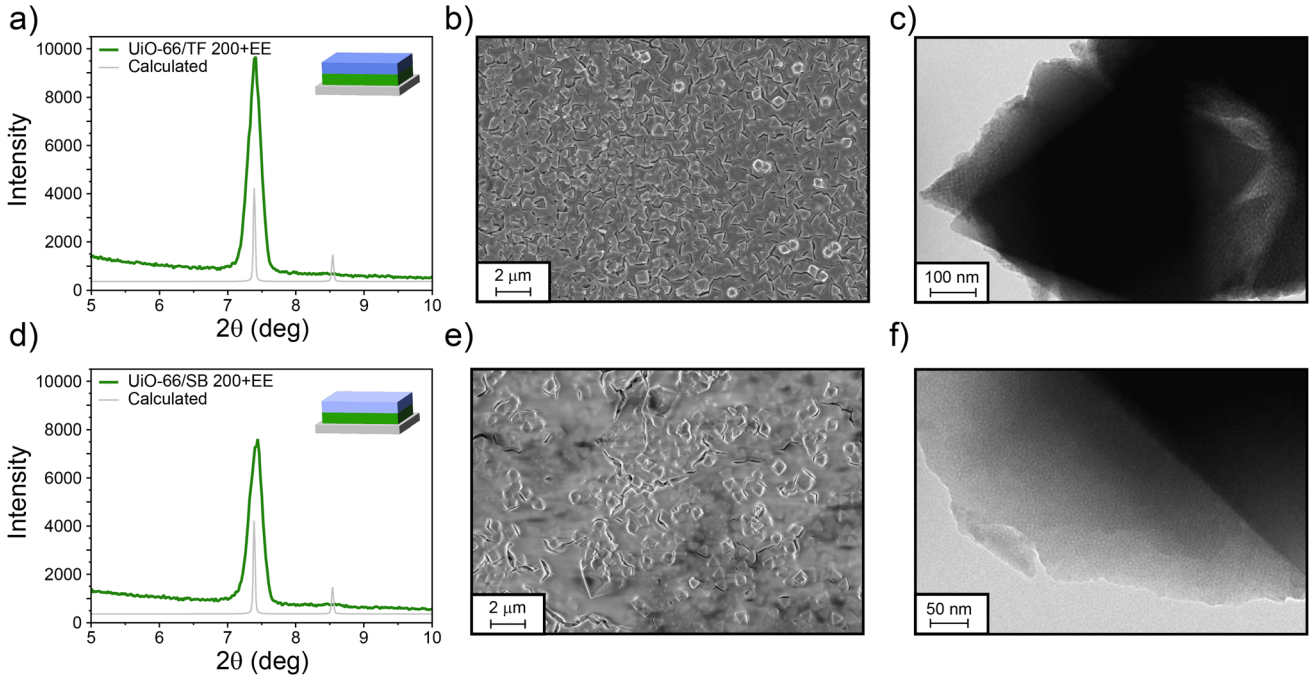

Fig. 5 GI-XRD pattern, SEM, and TEM images for UiO-66/TF 200+EE (a–c) and UiO-66/SB 200+EE (d–f) bilayers.

4. Conclusions

The results presented demonstrate the feasibility of obtaining bilayers based on ordered mesoporous oxides and UiO-66 MOF films, in both possible configurations: mesoporous thin films or UiO-66 in contact with the substrate. In these bilayers, the stratification is clear and both materials presented accessible porosity. Synthesis requires to slightly adapt MTF preparation conditions to ensure MOF thermal stability. The UiO-66 synthesis by LPE methodology, on the other hand, does not seem to be affected by the substrate used as the seed for the growth. In fact, UiO-66 films could be formed either on top of silicon, glass or calcined MTFs without a major change in their characteristics.

However, not all MOFs can be grown under conditions of compatibility with ordered mesoporous thin films. In particular, ZIF-8 films were not compatible and thus, stratified bilayers could not be obtained. When ZIF-8 was employed as the first layer, deposition of the MTF on top resulted in the elimination of the MOF. On the other hand, the growth or deposit of ZIF-8 on top of the MTF could not be achieved; in particular, when LPE conditions were used, the pores of the MTF were filled, affecting accessibility, which is undesirable for its use as a sensor.

The requirement of smoothness and controlled thickness remains a challenge; we have shown that while spin coating is suitable for MTFs, this is not strictly valid for the MOF layer. Although LPE synthesis of UiO-66 MOF yields reasonable smooth layers, a further degree of control is needed if multiple bilayers are to be obtained. We envision that recently proposed strategies for MOF synthesis and processing would allow this goal; *e.g.*, the use of Zr-clusters as seeds,[75] or colloidal suspensions of few-nanometer-thick MOF nanosheets obtained through doctor-blading.[76] In summary, our work demonstrates that by adequately choosing the MOF identity and the deposition conditions it is possible to obtain well stratified bilayers. We have demonstrated that the combination of MOFs and MTFs constitutes a viable option for building responsive 1D-PCs with hierarchical porosity and *ad hoc* chemical affinity.

Conflicts of interest

There are no conflicts to declare.

Acknowledgements

This work was supported by Agencia I+D+i (PICT 2019-01615 & PICT 2020-02549). The authors thank Gonzalo Zbihlei for his assistance in the TEM measurements. Authors are indebted to CONICET, UNLP and CNEA from Argentina for financial support.

References

1 P. Ganter and B. V. Lotsch, Photonic nanoarchitectonics with stimuli-responsive 2D materials, *Mol. Syst. Des. Eng.*, 2019, **4**, 566–579.
2 C. Fenzl, T. Hirsch and O. S. Wolfbeis, Photonic crystals for chemical sensing and biosensing, *Angew. Chem., Int. Ed.*, 2014, **53**, 3318–3335.
3 P. Lova, G. Manfredi and D. Comoretto, Advances in Functional Solution Processed Planar 1D Photonic Crystals, *Adv. Opt. Mater.*, 2018, **6**(24), 1800730.
4 J. F. Galisteo-Lõpez, *et al.*, Self-assembled photonic structures, *Adv. Mater.*, 2011, **23**, 30–69.

5 L. D. Bonifacio, *et al.*, Towards the photonic nose: A novel platform for molecule and bacteria identification, *Adv. Mater.*, 2010, **22**, 1351–1354.
6 Y. Shen, A. Tissot and C. Serre, Recent progress on MOF-based optical sensors for VOC sensing, *Chem. Sci.*, 2022, **13**, 13978–14007.
7 H. Xu, P. Wu, C. Zhu, A. Elbaz and Z. Z. Gu, Photonic crystal for gas sensing, *J. Mater. Chem. C*, 2013, **1**, 6087–6098.
8 Z. Hu, *et al.*, Fabrication of an NH2-MIL-88B photonic film for naked-eye sensing of organic vapors, *J. Mater. Chem. A*, 2014, **2**, 14222–14227.
9 S. Y. Choi, M. Mamak, G. Von Freymann, N. Chopra and G. A. Ozin, Mesoporous bragg stack color tunable sensors, *Nano Lett.*, 2006, **6**, 2456–2461.
10 T. L. Kelly, A. Garcia Sega and M. J. Sailor, Identification and quantification of organic vapors by time-resolved diffusion in stacked mesoporous photonic crystals, *Nano Lett.*, 2011, **11**, 3169–3173.
11 C. Boissiere, *et al.*, Porosity and mechanical properties of mesoporous thin films assessed by environmental ellipsometric porosimetry, *Langmuir*, 2005, **21**, 12362–12371.
12 C. J. Brinker, Y. Lu, A. Sellinger and H. Fan, Evaporation-Induced Self-Assembly: Nanostructures Made Easy, *Adv. Mater.*, 1999, **11**, 579–585.
13 P. Innocenzi and L. Malfatti, Mesoporous thin films: properties and applications, *Chem. Soc. Rev.*, 2013, **42**, 4198.
14 M. C. Fuertes, *et al.*, Photonic Crystals from Ordered Mesoporous Thin-Film Functional Building Blocks, *Adv. Funct. Mater.*, 2007, **17**, 1247–1254.
15 M. N. Ghazzal, O. Deparis, J. De Coninck and E. M. Gaigneaux, Tailored refractive index of inorganic mesoporous mixed-oxide Bragg stacks with bio-inspired hygrochromic optical properties, *J. Mater. Chem. C*, 2013, **1**, 6202.
16 B. Auguié, *et al.*, Tamm Plasmon Resonance in Mesoporous Multilayers: Toward a Sensing Application, *ACS Photonics*, 2014, **1**, 775–780.
17 M. Odziomek, F. Thorimbert, C. Boissiere, G. L. Drisko, S. Parola, C. Sanchez and M. Faustini, Periodic Nanoporous Inorganic Patterns Directly Made by Self-Ordering of Cracks, *Adv. Mater.*, 2022, **34**(36), 2204489.
18 J. Kobler, B. V. Lotsch, G. A. Ozin and T. Bein, Vapor-Sensitive Bragg Mirrors and Optical Isotherms from Mesoporous Nanoparticle Suspensions, *ACS Nano*, 2009, **3**, 1669–1676.
19 Z. Xie, *et al.*, An Optical Nose Chip Based on Mesoporous Colloidal Photonic Crystal Beads, *Adv. Mater.*, 2014, **26**, 2413–2418.
20 Z. Wang, *et al.*, Metal-organic framework-based photonic crystal platforms for gas sensing: a review, *Mater. Adv.*, 2022, **3**, 6728–6741.
21 B. F. Hoskins and R. Robson, Design and construction of a new class of scaffolding-like materials comprising infinite polymeric frameworks of 3D-linked molecular rods. A reappraisal of the zinc cyanide and cadmium cyanide structures and the synthesis and structure of the diamond-related frameworks $[N(CH_3)_4][CuIZnII(CN)_4]$ and CuI[4,4′,4″,4‴-tetracyanotetraphenylmethane]BF4·$x$$C_6H_5NO_2$, *J. Am. Chem. Soc.*, 1990, **112**, 1546–1554.
22 H. Li, M. Eddaoudi, T. L. Groy and O. M. Yaghi, Establishing Microporosity in Open Metal–Organic Frameworks: Gas Sorption Isotherms for Zn(BDC) (BDC = 1,4-Benzenedicarboxylate), *J. Am. Chem. Soc.*, 1998, **120**, 8571–8572.
23 S. E. Skrabalak and R. Vaidhyanathan, The Chemistry of Metal Organic Framework Materials, *Chem. Mater.*, 2023, **35**, 5713–5722.
24 P. Horcajada, *et al.*, Porous metal-organic-framework nanoscale carriers as a potential platform for drug deliveryand imaging, *Nat. Mater.*, 2010, **9**, 172–178.
25 W. Liang, *et al.*, Enhanced Activity of Enzymes Encapsulated in Hydrophilic Metal–Organic Frameworks, *J. Am. Chem. Soc.*, 2019, **141**, 2348–2355.
26 N. Hanikel, M. S. Prévot and O. M. Yaghi, MOF water harvesters, *Nat. Nanotechnol.*, 2020, **15**, 348–355.
27 M. A. Andrés, *et al.*, Methanol and Humidity Capacitive Sensors Based on Thin Films of MOF Nanoparticles, *ACS Appl. Mater. Interfaces*, 2020, **12**, 4155–4162.
28 I. Stassen, *et al.*, An updated roadmap for the integration of metal–organic frameworks with electronic devices and chemical sensors, *Chem. Soc. Rev.*, 2017, **46**, 3185–3241.
29 G. Laucirica, *et al.*, Switchable Ion Current Saturation Regimes Enabled *via* Heterostructured Nanofluidic Devices Based on Metal–Organic Frameworks, *Adv. Mater.*, 2022, **2207339**, 2207339.
30 O. Dalstein, *et al.*, Evaporation-Directed Crack-Patterning of Metal–Organic Framework Colloidal Films and Their Application as Photonic Sensors, *Angew. Chem., Int. Ed.*, 2017, **56**, 14011–14015.
31 G. Lu and J. T. Hupp, Metal-organic frameworks as sensors: A ZIF-8 based Fabry-Pérot device as a selective sensor for chemical vapors and gases, *J. Am. Chem. Soc.*, 2010, **132**, 7832–7833.
32 J. Fonseca, L. Meng, I. Imaz and D. Maspoch, Self-assembly of colloidal metal-organic framework (MOF) particles, *Chem. Soc. Rev.*, 2023, **52**, 2528–2543.
33 C. Liu, *et al.*, MOF-Based Photonic Crystal Film toward Separation of Organic Dyes, *ACS Appl. Mater. Interfaces*, 2020, **12**, 2816–2825.
34 F. Li, *et al.*, Metal-organic frameworks with a three-dimensional ordered macroporous structure: Dynamic photonic materials, *Angew. Chem., Int. Ed.*, 2011, **50**, 12518–12522.
35 C. Avci, *et al.*, Self-assembly of polyhedral metal-organic framework particles into three-dimensional ordered superstructures, *Nat. Chem.*, 2018, **10**, 78–84.
36 L. Bai, *et al.*, Responsive Amorphous Photonic Structures of Spherical/Polyhedral Colloidal Metal–Organic Frameworks, *Adv. Opt. Mater.*, 2019, **7**, 1–8.
37 A. Razmjou, *et al.*, Preparation of Iridescent 2D Photonic Crystals by Using a Mussel-Inspired Spatial Patterning of ZIF-8 with Potential Applications in Optical Switch and Chemical Sensor, *ACS Appl. Mater. Interfaces*, 2017, **9**, 38076–38080.

38 Z. Hu, C. A. Tao, F. Wang, X. Zou and J. Wang, Flexible metal-organic framework-based one-dimensional photonic crystals, *J. Mater. Chem. C*, 2015, **3**, 211–216.
39 G. Lu, *et al.*, Fabrication of metal-organic framework-containing silica-colloidal crystals for vapor sensing, *Adv. Mater.*, 2011, **23**, 4449–4452.
40 Z. Li, *et al.*, Photonic crystals constructed by isostructural metal-organic framework films, *Nano Res.*, 2023, **16**, 9569–9576.
41 Z. Li, *et al.*, Metal–Organic Frameworks-Based Fabry–Pérot Cavity Encapsulated TiO_2 Nanoparticles for Selective Chemical Sensing, *Adv. Funct. Mater.*, 2022, **32**, 1–9.
42 A. Von Mankowski, K. Szendrei-Temesi, C. Koschnick and B. V. Lotsch, Improving analyte selectivity by post-assembly modification of metal-organic framework based photonic crystal sensors, *Nanoscale Horiz.*, 2018, **3**, 383–390.
43 A. Ranft, F. Niekiel, I. Pavlichenko, N. Stock and B. V. Lotsch, Tandem MOF-based photonic crystals for enhanced analyte-specific optical detection, *Chem. Mater.*, 2015, **27**, 1961–1970.
44 O. Azzaroni and K. Ariga, *Concepts and Design of Materials Nanoarchitectonics*, The Royal Society of Chemistry, 2022.
45 O. Azzaroni and K. Ariga, *Materials Nanoarchitectonics: From Integrated Molecular Systems to Advanced Devices*, Elsevier B.V, 2024.
46 J. Winarta, *et al.*, A Decade of UiO-66 Research: A Historic Review of Dynamic Structure, Synthesis Mechanisms, and Characterization Techniques of an Archetypal Metal-Organic Framework, *Cryst. Growth Des.*, 2020, **20**, 1347–1362.
47 K. S. Park, *et al.*, Exceptional chemical and thermal stability of zeolitic imidazolate frameworks, *Proc. Natl. Acad. Sci. U. S. A.*, 2006, **103**, 10186–10191.
48 J. A. Allegretto, *et al.*, Impact of Chemical Primers on the Growth, Structure, and Functional Properties of ZIF-8 Films, *J. Phys. Chem. C*, 2022, **126**, 6724–6735.
49 D. F. Lionello, *et al.*, Structural and Mechanical Evolution of Mesoporous Films with Thermal Treatment: The Case of Brij 58 Templated Titania, *J. Phys. Chem. C*, 2017, **121**, 22576–22586.
50 E. L. Crepaldi, *et al.*, Controlled Formation of Highly Organized Mesoporous Titania Thin Films: From Mesostructured Hybrids to Mesoporous Nanoanatase TiO_2, *J. Am. Chem. Soc.*, 2003, **125**, 9770–9786.
51 A. Escobar, *et al.*, One-Step Synthesis of Mesoporous Silica Thin Films Containing Available COOH Groups, *ACS Omega*, 2017, **2**, 4548–4555.
52 S. Alberti, J. Giussi, O. Azzaroni and G. J. A. A. Soler-Illia, A Comparative Study of PMETAC-Modified Mesoporous Silica and Titania Thin Films for Molecular Transport Manipulation, *Polymers*, 2022, **14**, 4823.
53 J. A. Allegretto, *et al.*, Polyelectrolyte Capping As Straightforward Approach toward Manipulation of Diffusive Transport in MOF Films, *Langmuir*, 2018, **34**, 425–431.
54 J. A. Allegretto, *et al.*, Shedding Light on the Dark Corners of Metal–Organic Framework Thin Films: Growth and Structural Stability of ZIF-8 Layers Probed by Optical Waveguide Spectroscopy, *J. Phys. Chem. A*, 2019, **123**, 1100–1109.
55 J. Cravillon, *et al.*, Fast nucleation and growth of ZIF-8 nanocrystals monitored by time-resolved *in situ* small-angle and wide-angle X-ray scattering, *Angew. Chem., Int. Ed.*, 2011, **50**, 8067–8071.
56 C. Zhang, *et al.*, Defect-Controlled Preparation of UiO-66 Metal–Organic Framework Thin Films with Molecular Sieving Capability, *Chem.–Asian J.*, 2016, **11**, 207–210.
57 Y. Han, *et al.*, Facile synthesis of morphology and size-controlled zirconium metal–organic framework UiO-66: the role of hydrofluoric acid in crystallization, *CrystEngComm*, 2015, **17**, 6434–6440.
58 M. Kandiah, *et al.*, Synthesis and stability of tagged UiO-66 Zr-MOFs, *Chem. Mater.*, 2010, **22**, 6632–6640.
59 M. Athar, P. Rzepka, D. Thoeny, M. Ranocchiari and J. Anton van Bokhoven, Thermal degradation of defective high-surface-area UiO-66 in different gaseous environments, *RSC Adv.*, 2021, **11**, 38849–38855.
60 J. B. James and Y. S. Lin, Kinetics of ZIF-8 Thermal Decomposition in Inert, Oxidizing, and Reducing Environments, *J. Phys. Chem. C*, 2016, **120**, 14015–14026.
61 G. C. Shearer, *et al.*, Defect Engineering: Tuning the Porosity and Composition of the Metal–Organic Framework UiO-66 *via* Modulated Synthesis, *Chem. Mater.*, 2016, **28**, 3749–3761.
62 M. M. Zalduendo, *et al.*, Au Nanoparticles-Mesoporous TiO_2 Thin Films Composites as SERS Sensors: A Systematic Performance Analysis, *J. Phys. Chem. C*, 2018, **122**, 13095–13105.
63 M. C. Fuertes, M. Marchena, M. C. Marchi, A. Wolosiuk and G. J. A. A. Soler-Illia, Controlled Deposition of Silver Nanoparticles in Mesoporous Single- or Multilayer Thin Films: From Tuned Pore Filling to Selective Spatial Location of Nanometric Objects, *Small*, 2009, **5**, 272–280.
64 M. Klotz, V. Rouessac, D. Rébiscoul, A. Ayral and A. van der Lee, Adsorption–desorption isotherms of nanoporous thin films measured by X-ray reflectometry, *Thin Solid Films*, 2006, **495**, 214–218.
65 M. Rafti, *et al.*, Metal–organic frameworks meet polymer brushes: enhanced crystalline film growth induced by macromolecular primers, *Mater. Chem. Front.*, 2017, **1**, 2256–2260.
66 J. A. Allegretto, *et al.*, Growth of ZIF-8 MOF Films with Tunable Porosity by using Poly(1-vinylimidazole) Brushes as 3D Primers, *Chem.–Eur. J.*, 2020, **26**, 12388–12396.
67 S. Dourdain, J. F. Bardeau, M. Colas, B. Smarsly, A. Mehdi, B. M. Ocko and A. Gibaud, Determination by X-ray reflectivity and small angle X-ray scattering of the porous properties of mesoporous silica thin films, *Appl. Phys. Lett.*, 2005, **86**(11), 113108.
68 M. Miyamoto, S. Kohmura, H. Iwatsuka, Y. Oumi and S. Uemiya, In situ solvothermal growth of highly oriented Zr-based metal organic framework UiO-66 film with monocrystalline layer, *CrystEngComm*, 2015, **17**, 3422–3425.
69 M. C. Lawrence and M. J. Katz, Analysis of the Water Adsorption Isotherms in UiO-Based Metal–Organic Frameworks, *J. Phys. Chem. C*, 2022, **126**, 1107–1114.

70 G. J. A. A. Soler-Illia, P. C. Angelomé, M. C. Fuertes, D. Grosso and C. Boissiere, Critical aspects in the production of periodically ordered mesoporous titania thin films, *Nanoscale*, 2012, **4**, 2549.
71 M. Fernanda Torresan, *et al.*, Emissive Platforms Employing NaYF 4 -based Upconverting Nanoparticles and Mesoporous Metal Oxide Thin Films, *Eur. J. Inorg. Chem.*, 2021, **2021**, 2343–2352.
72 J. H. Cavka, *et al.*, A new zirconium inorganic building brick forming metal organic frameworks with exceptional stability, *J. Am. Chem. Soc.*, 2008, **130**, 13850–13851.
73 L. Valenzano, *et al.*, Disclosing the complex structure of UiO-66 metal organic framework: A synergic combination of experiment and theory, *Chem. Mater.*, 2011, **23**, 1700–1718.
74 D. Rodríguez-Fernández, P. C. Angelomé, G. J. A. A. Soler-Illia and L. M. Liz-Marzán, Multilayered Materials Comprising Mesoporous Thin Films and Metal Nanoparticles, *Part. Part. Syst. Charact.*, 2017, **34**, 1600428.
75 R. T. Jerozal, T. A. Pitt, S. N. MacMillan and P. J. Milner, High-Concentration Self-Assembly of Zirconium- and Hafnium-Based Metal–Organic Materials, *J. Am. Chem. Soc.*, 2023, **145**, 13273–13283.
76 H. Yuan, K. Li, D. Shi, H. Yang, X. Yu, W. Fan, D. Zhao, *et al.*, Large-Area Fabrication of Ultrathin Metal-Organic Framework Membranes, *Adv. Mater.*, 2023, **35**(18), 2211859.
77 C. Duan, K. Liang, J. Lin, J. Li, L. Li, L. Kang, Y. Yu and H. Xi, Application of hierarchically porous metal-organic frameworks in heterogeneous catalysis: A review, *Sci. China Mater.*, 2022, **65**, 298–320.